Electron scattering from the molecular hydrogen ion and its isotopologues

Mark C. Zammit,* Dmitry V. Fursa, and Igor Bray
ARC Centre for Antimatter-Matter Studies, Curtin University, GPO Box U1987, Perth, WA 6845, Australia
(Received 18 June 2014; published 18 August 2014)

We have extended the *ab initio* convergent close-coupling method to electron scattering from the vibrationally excited molecular hydrogen ion and its isotopologues. Calculations have been performed within the adiabatic-nuclei approximation. Results are presented for dissociative excitation and ionization as a function of the initial vibrational state of the molecules. Comparison with experiment is excellent across the energy range from near threshold to 1 keV.

DOI: 10.1103/PhysRevA.90.022711 PACS number(s): 34.80.Gs, 34.50.Fa, 52.20.Fs

I. INTRODUCTION

Electron collisions with the H_2^+, H_2, and H_3^+ molecules play an important role in determining the dynamics of astrophysical and laboratory produced low-temperature hydrogen plasmas [1]. Physical conditions for the sustainability of molecular systems are found on the edge of magnetically confined plasmas, and can account for the dominant electron-ion inelastic collision processes. Hence, collision data for H_2^+ and it isotopologues (D_2^+, T_2^+, HD^+, HT^+, and DT^+) are important in the modeling of fusion plasmas. The simplest molecule H_2^+ is of fundamental interest to theorists in the study of electron-molecule scattering, photoionization of molecular hydrogen and dissociative excitation, recombination and ionization processes.

Electron scattering from the electronic ground $1s\sigma_g$ state of H_2^+ in a vibrational state v is described by the following dissociative reactions:

$$e^- + H_2^+(1s\sigma_g, v) \rightarrow 2e^- + H^+ + H^+, \quad \text{dissociative ionization (DI)} \tag{1}$$

$$\rightarrow e^- + H_2^{+*} \rightarrow e^- + H^+ + H(nl), \quad \text{dissociative excitation (DE)} \tag{2}$$

$$\rightarrow H_2^{**} \rightarrow e^- + H^+ + H(nl), \quad \text{resonant dissociative excitation} \tag{3}$$

$$\rightarrow H_2^{**} \rightarrow H(nl) + H(n'l'), \quad \text{dissociative recombination (DR)} \tag{4}$$

$$\rightarrow H_2^{**} \rightarrow H^+ + H^-, \quad \text{resonant ion pair production,} \tag{5}$$

where H_2^{+*} indicates an excited state of H_2^+, and H_2^{**} is either a doubly excited or autoionizing Rydberg state of H_2 with the respective dissociative asymptotic conditions. Autoionization into the H_2^+ continuum results in resonant dissociative excitation (3), while the population which survives dissociates in the vibrational continuum of H_2 and produces two neutral hydrogen atoms (4) [1]. In the low-energy region ($\leqslant$10 eV), indirect resonant electron attachment processes (3), (4), and (5) are important, while in the intermediate- and high-energy regions the direct processes (1) and (2) are dominant [2].

Many experiments [3–7] of electron scattering from H_2^+ have measured proton production (PP) cross sections $\sigma_{PP} = \sigma_{DE} + 2\sigma_{DI}$. Total inelastic (TI) cross sections $\sigma_{TI} = \sigma_{DE} + \sigma_{DI}$ and σ_{DE} have been measured by Peart and Dolder [8,9,10] across a wide range of energies. The low-energy region has been investigated by Hus *et al.* [11], Yousif and Mitchell [12], and Andersen *et al.* [13]. In the low-energy region, large variation of the measured DE, PP, and TI cross sections is primarily due to the production of H_2^+ in different vibrational states and other reasons pointed out by Peart and Dolder [8]. DI cross sections have been measured by Peart and Dolder [14] and El Ghazaly *et al.* [7] from 20 to 3000 eV. It is important to note that the DI cross sections [7,14] are an order of magnitude lower than the PP cross sections, and are smaller than the experimental error bars of σ_{PP} [3–6]. Hence, measurements of DE, PP, or TI cross sections can be compared with each other.

Experimentally, H_2^+ is produced by electron- or photon-impact ionization of H_2, which can leave H_2^+ in one of its 20 bound vibrational states. Due to the lack of dipole moment of H_2^+ (homonuclear-diatomic), relaxation of these states via dipole transitions is forbidden and they have long lifetimes. Hence, many experimental measurements are taken with H_2^+ populated in a range of vibrational states [15]. Calculations of Peek [16] showed that the PP cross sections have a strong dependence on the vibrational population and can affect the DE cross section as much as two orders of magnitude [16]. Theoretical [15] and experimental [17,18] investigations have been conducted to determine the initial vibrational populations of H_2^+. The series of measurements performed by Peart and Dolder [8,9,14], Dunn *et al.* [3], Dance *et al.* [5], and Dunn and Van Zyl [4] were designed to have a H_2^+ ion beam source with an initial vibration population given by the Franck-Condon (FC) factors. Peart and Dolder [14] suggested to use the experimentally determined distribution of von Busch and Dunn [15], which better describes experimental conditions. The von Busch and Dunn [15] (BD) distribution

*mark.zammit@postgrad.curtin.edu.au

was produced by a least-squares fit of vibrationally resolved photodissociation cross sections of H_2^+ to their measurements. The BD distribution is smooth, close to the FC factors and are thought to account for the coupling between electronic and nuclear motion. The most recent experiment of El Ghazaly *et al.* [7] measured their ion beam source vibrational level distribution via resolution of the kinetic energy release spectrum of the protons. This showed good agreement with the FC and BD distributions. At the Aarhus Storage Ring in Denmark, ions can be stored for tens of seconds allowing control over the ions' vibrational distribution. Measurements of DE have been conducted with a laser-controlled ion beam which produced HD^+ in $v = 0$ and H_2^+ in $v = 0$ and 1 vibrational states [13].

Until recently, the only theoretical investigations into electron scattering from H_2^+ and its isotopologues were conducted by first- or second-order approaches. Adiabatic-nuclear calculations of the electron-H_2^+ system within the first Born [16,19,20] and Bethe-Born [20] approximations found that the direct DE cross section has a strong dependence on the vibrational state v. Peek [16] showed that the DE cross sections increase monotonically with increasing v and become dramatically large for highly excited vibrational states. Peek [16,19,20] also used and validated closure methods (summing cross sections over final rotational-vibrational states) in the Born approximation [21]. Liu [22] used the Bethe theory combined with the reflection approximation to obtain vibrationally weighted PP, DI, and DE cross sections assuming the BD or FC distributions. In the reflection (sometimes known as the delta) approximation, the nuclear wave function is approximated by a delta function [23] with appropriate energy normalization conditions [24]. These methods [20,22] accounted for direct processes only, and vibrationally weighted results compared well with experimental PP and DI data at high energies. The modified binary-encounter-Bethe model (referred to as BEQ) has been used by NIST to obtain DI cross sections [25].

The multichannel quantum defect theory (MQDT) is a perturbative method used to calculate low-energy direct and indirect DE and DR cross sections [2,26–28]. Fifirig and Stroe [2] and Takagi [26] have calculated DE cross sections for each vibrational state of H_2^+ and found that DE cross sections monotonically increase up to $v = 9$ and then begin to decrease. Fifirig and Stroe [2] results for DR were in good agreement with the measurements of Andersen *et al.* [13], however, their DE cross sections underestimated experimental data. Recent calculations of Chakrabarti *et al.* [28] produced DR cross sections of HD^+ in reasonable agreement with experiment and relied on data supplied by Tennyson [29], who used the R-matrix method to calculate resonance parameters [30].

The distorted-wave method of Robicheaux [31] utilized the fixed-nuclei approximation to calculate DI cross sections. Robicheaux [31] used a fixed-nuclear distance of $R = 2.15\,a_0$, which is the average distance of H_2^+ according to the BD vibrational distribution [15]. Recently, the fixed-nuclei (equilibrium distance $R = 2.0\,a_0$) approximation was utilized in the time-dependent close-coupling (TDCC) method [32] and configuration-average distorted-wave (CADW) method [33] to calculate DI cross sections. Although these calculations [31–33] compared well with the experiment of Peart and Dolder [14], they did not take into account the initial vibrational distribution of molecular states. The recent application of the adiabatic convergent close-coupling (CCC) method [34] showed that the initial vibrational distribution leads to a substantial increase in the DI and PP cross sections.

The *ab initio* CCC method was originally developed to provide accurate collision data for electron scattering from hydrogenlike atoms and ions [35,36]. It was then extended to more complex scattering systems [37–41], relativistic targets [42–44], and heavy projectiles [45]. Our long-term goal is to do the same for molecular targets. Recently, the CCC method was extended to electron [34], positron [46], and antiproton [47,48] scattering from diatomic molecules, which produced results in good agreement with experiment over a broad energy range. The purpose of this paper is to give full details of the molecular CCC method used in the investigation of electron scattering from the vibrationally excited molecular hydrogen ion H_2^+ [34], and present new and improved results for H_2^+ and its isotopologues. We investigate the direct DE and DI cross-section dependence on the initial vibrational state of H_2^+ and its isotopologues within the adiabatic-nuclei approximation. The formulation presented here relies on the Born-Oppenheimer approximation and is a general method that can be applied to quasi-one-electron diatomic molecules and their isotopologues.

II. METHOD

Application of the convergent close-coupling (CCC) method to molecules involves solution of the electronic Lippmann-Schwinger equation at fixed internuclear distances. Utilizing the adiabatic-nuclei approximation account of the initial vibrational levels is performed as "post processing" of fixed-nuclei scattering results and requires calculations to be conducted at a (large) number of internuclear distances. Initial vibrational state cross sections are obtained and weighted according to FC and BD distributions for H_2^+ and its isotopologues. This method does not retain energy conservation, however, it has been shown to be suitable for the H_2^+ molecule in the intermediate- and high-energy regions [49].

The H_2^+, D_2^+, T_2^+, HD^+, HT^+, and DT^+ systems are electronically equivalent within the Born-Oppenheimer approximation. For simplicity, we refer to H_2^+ when describing electronic properties of all these molecules. All equations are formulated in the body frame using a single-center spherical coordinate system, where we set the origin at the midpoint between the two nuclei and align the z axis along the internuclei axis $\boldsymbol{R}$. Relativistic effects are assumed to be negligible. Atomic units are used throughout the paper.

A. Target states

In the Born-Oppenheimer approximation, the molecular wave function is expressed in the form

$$\bar{\Phi}_{nvJ}(\boldsymbol{r},\boldsymbol{R}) = \Xi_{nvJ}(\boldsymbol{R})\Phi_n(\boldsymbol{r};\boldsymbol{R}), \tag{6}$$

where a molecular state $\bar{\Phi}_{nvJ}(\boldsymbol{r},\boldsymbol{R})$ is characterized by the electronic state n, vibrational quantum number v, and rotational quantum number J. Utilizing the Born-Oppenheimer approximation, the electronic wave function $\Phi_n(\boldsymbol{r};\boldsymbol{R})$ is

calculated at a fixed internuclear distance R. The electronic H_2^+ target Hamiltonian H_T describes an electron in the Coulomb potential of two protons that are fixed at a distance R. H_T is written as

$$H_T = H_1 + 1/R, \tag{7}$$

where

$$H_i = K_i(r_i) + V_i(\boldsymbol{r_i}, \boldsymbol{R}), \tag{8}$$

$$K_i(r_i) = -\frac{1}{2}\frac{d^2}{dr_i^2} + \frac{l(l+1)}{2r_i^2}, \tag{9}$$

$$V_i(\boldsymbol{r_i}, \boldsymbol{R}) = -\left(\frac{Z}{\left|\boldsymbol{r_i} + \frac{\boldsymbol{R}}{2}\right|} + \frac{Z}{\left|\boldsymbol{r_i} - \frac{\boldsymbol{R}}{2}\right|}\right), \tag{10}$$

Z is the charge of the individual nuclei (in this case $Z = 1$) and $1/R$ is the internuclear Coulomb repulsion. The potential (10) can be expanded in terms of partial waves

$$V_i(\boldsymbol{r_i}, \boldsymbol{R}) = -2Z \sum_{\lambda=0,2,4,\ldots}^{\infty} \sqrt{\frac{4\pi}{(2\lambda+1)}} v_\lambda(r_i, R/2) Y_{\lambda 0}(\hat{\boldsymbol{r}}_i), \tag{11}$$

where $v_\lambda(r_i, r_j) = r_<^\lambda / r_>^{\lambda+1}$, $r_< = \min(r_i, r_j)$, and $r_> = \max(r_i, r_j)$.

Electronic target states of H_2^+ are characterized by the projection of orbital angular momentum m and parity π. For each combination of m and π, the target Hamiltonian (7) is diagonalized using a set of one-electron orbitals

$$\phi_j(\boldsymbol{r}) = \frac{1}{r}\varphi_{k_j l_j}(r) Y_{l_j m_j}(\hat{\boldsymbol{r}}), \tag{12}$$

with $m_j = m$ and $(-1)^{l_j} = \pi$. The radial functions $\varphi_{k_j l_j}(r)$ are the Laguerre functions

$$\varphi_{kl}(r) = \sqrt{\frac{\alpha_l (k-1)!}{(k+l)(k+2l)!}} (2\alpha_l r)^{l+1} \times \exp(-\alpha_l r) L_{k-1}^{2l+1}(2\alpha_l r), \tag{13}$$

where α_l is the exponential falloff parameter, L_{k-1}^{2l+1} are the associated Laguerre polynomials, and k ranges from 1 to N_l. Matrix elements of the target Hamiltonian (7) are evaluated using analytic properties of the Laguerre basis functions [50], which have been extensively used in the J-matrix method [51]. Upon diagonalization of (7), a total of N electronic target states with energy ε_n can be generated, where

$$\Phi_n^{m\pi}(\boldsymbol{r}) = \sum_{j=1}^{N} C_j^{(n)} \phi_j(\boldsymbol{r}), \tag{14}$$

and satisfy

$$\langle \Phi_{n'} | H_T | \Phi_n \rangle = \varepsilon_n \delta_{n',n}. \tag{15}$$

The multicenter nature of H_2^+ leads to a slow convergence rate of the calculated wave functions with respect to the orbital angular momentum l of the Laguerre functions, in particular, for the $1s\sigma_g$ ground state and $2p\sigma_u$ excited state. To improve accuracy and save on computational resources, structure calculations are performed in two steps. First, a large Laguerre basis is used to diagonalize the target Hamiltonian (7) and generate accurate $1s\sigma_g$ and $2p\sigma_u$ states of H_2^+. Second, a new Laguerre basis is produced with the same values of exponential falloffs but smaller values of l and N_l. Then, the $1s\sigma_g$ and $2p\sigma_u$ orbitals of this new basis are replaced with the $1s\sigma_g$ and $2p\sigma_u$ states calculated at the first step. This new basis is used to diagonalize the target Hamiltonian (7) and generate electronic states that are then used in scattering calculations. The lack of spherical symmetry of the system leads to a substantial increase in the number of states generated when compared to the atomic case for the same size of the Laguerre basis (13).

By calculating the electronic target states of H_2^+ at various R and interpolating, potential energy curves $\varepsilon_n(R)$ are obtained. The total Born-Oppenheimer Hamiltonian is formed:

$$H_n^{\mathrm{BO}} = K_1^{\mathrm{Nuc}} + K_2^{\mathrm{Nuc}} + \varepsilon_n(R) = -\frac{1}{2M_1}\nabla_1^2 - \frac{1}{2M_2}\nabla_2^2 + \varepsilon_n(R), \tag{16}$$

where M_i is the mass of the individual nuclei; $M_i = 1836.152$ for a proton, $M_i = 3670.483$ for deuteron, and $M_i = 5496.922$ for triton. Nuclear wave functions $\Xi_{nvJ}(\boldsymbol{R})$ of the electronic ground state are calculated via diagonalization of the total Hamiltonian (16) for each J using a set of nuclear orbitals

$$\phi_j(\boldsymbol{R}) = \frac{1}{R}\varphi_{k_j J_j}(R) Y_{J_j m_j}(\hat{\boldsymbol{R}}). \tag{17}$$

Here, $\varphi_{k_j J_j}(R)$ are Laguerre basis functions (13) and the number of functions used in the diagonalization of (16) were taken to convergence. For the current study, we assume a nonrotating molecule and have $J = 0$.

B. Coupled T-matrix equations

We start with the body-frame electronic Schrödinger equation of the scattering system for a fixed internuclear distance R

$$(E^{(+)} - H)\left|\Psi_i^{S(+)}\right\rangle = 0, \tag{18}$$

where E is the total energy of the scattering system, $(+)$ denotes outgoing spherical-wave boundary conditions, S is the total spin, and i denotes the initial state of the system. Here, we omit notation for the dependence on R unless it is explicitly indicated. Ignoring kinetic energy of the nuclei (assuming infinite mass) in the current formalism, the full scattering Hamiltonian is defined as

$$H = H_0 + H_1 + V_{01} + 1/R, \tag{19}$$

where V_{01} is the electron-electron potential

$$V_{01} = \frac{1}{|\boldsymbol{r_0} - \boldsymbol{r_1}|} = \sum_{\lambda\mu}^{\infty} (-1)^\mu \frac{4\pi}{(2\lambda+1)} v_\lambda(r_0, r_1) Y_{\lambda-\mu}(\hat{\boldsymbol{r}}_0) Y_{\lambda\mu}(\hat{\boldsymbol{r}}_1), \tag{20}$$

and indices 0 and 1 denote the projectile and target coordinate space, respectively.

The close-coupling method utilizes the explicitly antisymmetrized multichannel expansion to expand the total wave function $\Psi_i^{S(+)}(\boldsymbol{r_0}, \boldsymbol{r_1})$ over the complete set of positive- and

negative-energy pseudostates $\Phi_n^N(\boldsymbol{r_1})$ of the target electron

$$\Psi_i^{SN(+)}(\boldsymbol{r_0},\boldsymbol{r_1}) = \left[1+(-1)^S P_{\boldsymbol{r_0},\boldsymbol{r_1}}\right]\sum_{n=1}^{N}\Phi_n^N(\boldsymbol{r_1})f_{ni}^{SN}(\boldsymbol{r_0}) = \left[1+(-1)^S P_{\boldsymbol{r_0},\boldsymbol{r_1}}\right]\psi_i^{SN(+)}(\boldsymbol{r_0},\boldsymbol{r_1}), \quad (21)$$

where $P_{\boldsymbol{r_0},\boldsymbol{r_1}}$ is the space exchange operator and $f_{ni}^{SN}(\boldsymbol{r_0})$ are the multichannel functions. However, expression (21) is too general and leads to nonunique solutions. This is a purely numerical problem that has been addressed for atomic and ionic targets [35,36]; a similar technique is applied to molecules. The following condition is enforced:

$$\langle\Phi_m^N|f_{ni}^{SN}\rangle = (-1)^S\langle\Phi_n^N|f_{mi}^{SN}\rangle, \quad (22)$$

to make $\psi_i^{SN(+)}(\boldsymbol{r_0},\boldsymbol{r_1})$ antisymmetric like $\Psi_i^{SN(+)}(\boldsymbol{r_0},\boldsymbol{r_1})$ but only within the space spanned by the target states. Condition (22) leads to the following property:

$$(-1)^S\langle\boldsymbol{k}^{(-)}{}_f\Phi_f^N|P_{\boldsymbol{r_0},\boldsymbol{r_1}}|\psi_i^{SN(+)}\rangle = \langle\boldsymbol{k}^{(-)}{}_f\Phi_f^N|I_0^N|\psi_i^{SN(+)}\rangle, \quad (23)$$

which is implemented within the energy term of the V-matrix elements

$$\begin{aligned}&(-1)^S E\langle\boldsymbol{k}^{(-)}{}_f\Phi_f^N|P_{\boldsymbol{r_0},\boldsymbol{r_1}}|\psi_i^{SN(+)}\rangle\\ &= (-1)^S(1-\theta+\theta)E\langle\boldsymbol{k}^{(-)}{}_f\Phi_f^N|P_{\boldsymbol{r_0},\boldsymbol{r_1}}|\psi_i^{SN(+)}\rangle\\ &= (-1)^S(1-\theta)E\langle\boldsymbol{k}^{(-)}{}_f\Phi_f^N|P_{\boldsymbol{r_0},\boldsymbol{r_1}}|\psi_i^{SN(+)}\rangle\\ &\quad+\theta E\langle\boldsymbol{k}^{(-)}{}_f\Phi_f^N|I_0^N|\psi_i^{SN(+)}\rangle. \end{aligned} \quad (24)$$

Here, I_0^N is the projection operator built from target states in the coordinate space of the projectile

$$I_0^N = \sum_n^N |\Phi_n^N\rangle\langle\Phi_n^N|. \quad (25)$$

The scattering system asymptotic Hamiltonian is chosen as

$$H_{\rm asy} = H_T + K_0 - Z_{\rm ion}/r_0 + U_0. \quad (26)$$

For this choice of $H_{\rm asy}$ the interaction potential is

$$V_U^{SN}(\theta) = V_0 + Z_{\rm ion}/r_0 - U_0 + V_{01} - E\theta I_0^N - (-1)^S[E(1-\theta)-H]P_{\boldsymbol{r_0},\boldsymbol{r_1}}, \quad (27)$$

where term (24) and hence condition (22) are implemented within the V-matrix elements. In Eqs. (26) and (27), U_0 is a short-ranged distorting potential that can lead to a number of projectile bound states. Choices of U_0 will be discussed later. For ionic targets, there are an infinite number of projectile bound states. These bound states are included into the Green's function until convergence is reached. Note that though V-matrix elements have a dependence on an arbitrary θ, the resultant on-shell T-matrix elements do not. Further discussion of this method can be found in [35,52].

Utilizing the Green's function approach, the Schrödinger equation (18) is transformed to the momentum-space Lippmann-Schwinger equation. Premultiplying by $\langle\boldsymbol{k}^{(-)}{}_f\Phi_f^N|V_U^{SN}(\theta)$, the coupled Lippmann-Schwinger equation for the distorted-wave T matrix is obtained

$$\langle\boldsymbol{k}^{(-)}{}_f\Phi_f^N|T_U^{SN}|\Phi_i^N\boldsymbol{k}^{(+)}{}_i\rangle = \langle\boldsymbol{k}^{(-)}{}_f\Phi_f^N|V_U^{SN}(\theta)|\Phi_i^N\boldsymbol{k}^{(+)}{}_i\rangle + \sum_{n=1}^{N}\sum\!\!\!\!\!\!\int_k d^3k\,\frac{\langle\boldsymbol{k}^{(-)}{}_f\Phi_f^N|V_U^{SN}(\theta)|\Phi_n^N\boldsymbol{k}^{(-)}\rangle\langle\boldsymbol{k}^{(-)}\Phi_n^N|T_U^{SN}|\Phi_i^N\boldsymbol{k}^{(+)}{}_i\rangle}{E^{(+)}-\varepsilon_k-\varepsilon_n^N+i0}, \quad (28)$$

where the distorted waves $|\boldsymbol{k}^{(\pm)}\rangle$ are solutions of the equation

$$(\varepsilon_k^{(\pm)} - K_0 + Z_{\rm ion}/r_0 - U_0)|\boldsymbol{k}^{(\pm)}\rangle = 0, \quad (29)$$

f denotes the final state of the system, and $\langle\boldsymbol{k}^{(-)}{}_f\Phi_f^N|T_U^{SN}|\Phi_i^N\boldsymbol{k}^{(+)}{}_i\rangle = \langle\boldsymbol{k}^{(-)}{}_f\Phi_f^N|V_U^{SN}(\theta)|\psi_i^{SN(+)}\rangle$. Noting that the distorted-wave T matrix is defined for the potential $V_U^{SN}(\theta) = V^{SN}(\theta) - U_0$, the physical T matrix T^{SN} is extracted via the relation [36]

$$\begin{aligned}&\langle\boldsymbol{q}^{(-)}{}_f\Phi_f^N|T^{SN}|\Phi_i^N\boldsymbol{q}^{(+)}{}_i\rangle\\ &\equiv\langle\boldsymbol{q}^{(-)}{}_f\Phi_f^N|V^{SN}|\psi_i^{SN(+)}\rangle\\ &= \langle\boldsymbol{k}^{(-)}{}_f\Phi_f^N|T_U^{SN}|\Phi_i^N\boldsymbol{k}^{(+)}{}_i\rangle + \delta_{f,i}\langle\boldsymbol{k}^{(-)}{}_f|U_0|\boldsymbol{q}^{(+)}{}_i\rangle, \end{aligned} \quad (30)$$

where $\boldsymbol{q}^{(\pm)}$ is a Coulomb wave. The method described here is also suitable for asymptotically neutral targets by taking $Z_{\rm ion} = 0$.

C. Solving the coupled Lippmann-Schwinger equation

It is our aim to perform accurate and large-scale multichannel calculations, so it is important to minimize the computational resources required. A partial-wave expansion of the projectile wave function can greatly reduce the computational resource required for solving (28). The distorted-wave partial-wave expansion is

$$|\boldsymbol{k}^{(\pm)}\rangle = \frac{\sqrt{2}}{kr\sqrt{\pi}}\sum_{L,M} i^L e^{\pm i(\sigma_L+\delta_L)}u_L(r;k;Z_{\rm ion})Y_{LM}(\hat{\boldsymbol{r}})Y_{LM}^*(\hat{\boldsymbol{k}}), \quad (31)$$

where σ_L and δ_L are the Coulomb and distorting phase shifts, respectively.

Utilising the partial-wave expansion of the projectile wave function (31), the coupled Lippmann-Schwinger equation for the distorted-wave T matrix is solved by expanding (28) in partial waves, which leads to the conservation of total angular projection M, parity Π, and spin S of the scattering system. For an incident electron with linear momentum k_i, orbital angular momentum L_i, and angular projection M_i, the partial-wave expansion for the V (or T) matrix

leads to

$$\left\langle \boldsymbol{k}^{(-)}{}_f\Phi_f^N\middle|V_U^{SN}(\theta)\middle|\Phi_i^N\boldsymbol{k}^{(\pm)}{}_i\right\rangle = (k_f k_i)^{-1}\sum_{\substack{L_f,L_i\\M_f,M_i}} i^{L_i-L_f}e^{i(\sigma_{L_f}+\delta_{L_f}\pm\sigma_{L_i}\pm\delta_{L_i})} \times V^{M\Pi S}_{fL_fM_f,iL_iM_i}(k_f,k_i)Y_{L_fM_f}\left(\hat{\boldsymbol{k}}_f^{\mathrm{B}}\right)Y^*_{L_iM_i}\left(\hat{\boldsymbol{k}}_i^{\mathrm{B}}\right), \quad (32)$$

where $V^{M\Pi S}_{fL_fM_f,iL_iM_i}(k_f,k_i)$ are the real V-matrix elements, $M = M_f + m_f = m_i + M_i$, $\Pi = \pi_f(-1)^{L_f} = \pi_i(-1)^{L_i}$, and $\hat{\boldsymbol{k}}^{\mathrm{B}}$ refers to the electron momentum vector in the body frame. Substituting Eq. (32) into the Lippmann-Schwinger equation (28), complex phases $i^{L_i-L_f}e^{i(\sigma_{L_f}+\delta_{L_f}\pm\sigma_{L_i}\pm\delta_{L_i})}$, constants $(k_fk_i)^{-1}$, and angular functions $Y_{L_fM_f}(\hat{\boldsymbol{k}}_f^{\mathrm{B}})Y^*_{L_iM_i}(\hat{\boldsymbol{k}}_i^{\mathrm{B}})$ can be factored out and the partial-wave Lippmann-Schwinger equation for the distorted-wave T matrix can be written as

$$T^{M\Pi S}_{fL_fM_f,iL_iM_i}(k_f,k_i) = V^{M\Pi S}_{fL_fM_f,iL_iM_i}(k_f,k_i) + \sum_{n=1}^{N}\sum_{L'M'}\int\!\!\!\!\!\!\diagup dk\,\frac{V^{M\Pi S}_{fL_fM_f,nL'M'}(k_f,k)T^{M\Pi S}_{nL'M',iL_iM_i}(k,k_i)}{E^{(+)}-\varepsilon_k-\varepsilon_n+i0}. \quad (33)$$

Equation (33) is efficiently solved using the standard techniques discussed in [35,36,43]. The loss of total angular momentum conservation in Eq. (33) is the major difference between solving Eq. (33) for diatomic molecules and atoms. This results in very large V-matrix arrays, which in the present calculations take ≈160 GB of memory for the first few values of M.

When evaluating the Lippmann-Schwinger equation, it is numerically favorable to have the most detailed structure of the integrand in the smaller values of k. As Z increases, the projectile-nuclei term V_0 in Eq. (27) is responsible for making the V-matrix elements go out further with respect to momentum k. To minimize this numerical issue, a short-ranged distorting potential U_0 is chosen such that it cancels the spherical part of the V_0 potential. Here, the distorting potential is defined as

$$U_0 = -2Zv_0(r_0,R/2) + \frac{Z_{\mathrm{ion}}}{r_0} + \int d^3r_1|\Phi_n(\boldsymbol{r_1})|^2v_0(r_0,r_1), \quad (34)$$

where n is typically the electronic ground state. This form of U_0 is spherically symmetric, short ranged, and ensures the shortest-range V-matrix elements by removing the projectile-nuclei term V_0 for the $\lambda = 0$ partial wave [referring to Eq. (11)]. The use of a short-ranged distorting potential is a purely numerical technique which saves on computational resources when solving the integral in Eq. (28). Results of T^{SN} from Eq. (30) must be independent of U_0.

Distorted-wave T-matrix elements are used to obtain physical ($U_0 = 0$) T-matrix elements $T^{M\Pi S}_{fL_fM_f,iL_iM_i}(q_f,q_i)$ via Eq. (30):

$$T^{M\Pi S}_{fL_fM_f,iL_iM_i}(q_f,q_i) = T^{M\Pi S}_{fL_fM_f,iL_iM_i}(k_f,k_i)e^{i(\delta_{L_i}+\delta_{L_f})} - \delta_{f,i}\delta_{L_f,L_i}\delta_{M_f,M_i}q_i\pi^{-1}e^{i\delta_{L_i}}\sin(\delta_{L_i}), \quad (35)$$

where q is the linear momentum of the electron and indicates the physical T-matrix elements. The physical T matrix can then be expressed as

$$\left\langle \boldsymbol{q}^{(-)}{}_f\Phi_f^N\middle|T^{SN}\middle|\Phi_i^N\boldsymbol{q}^{(+)}{}_i\right\rangle = (q_fq_i)^{-1}\sum_{\substack{L_f,L_i\\M_f,M_i}} i^{L_i-L_f}e^{i(\sigma_{L_i}+\sigma_{L_f})} \times T^{M\Pi S}_{fL_fM_f,iL_iM_i}(q_f,q_i)Y_{L_fM_f}\left(\hat{\boldsymbol{q}}_f^{\mathrm{B}}\right)Y^*_{L_iM_i}\left(\hat{\boldsymbol{q}}_i^{\mathrm{B}}\right). \quad (36)$$

These physical body-frame T-matrix elements are used to obtain orientationally averaged cross sections.

D. Scattering amplitudes and analytic Born subtraction method

Body-frame scattering amplitudes

$$F^S_{f,i}(\Omega^{\mathrm{B}}) = -(2\pi)^2\left\langle \boldsymbol{q}^{(-)}{}_f\Phi_f^N\middle|T^{SN}\middle|\Phi_i^N\boldsymbol{q}^{(+)}{}_i\right\rangle \quad (37)$$

are rotated to align the incoming electron momentum $\hat{\boldsymbol{q}}_i^{\mathrm{B}}$ with the laboratory-frame z axis. The following definitions

$$Y_{LM}(\hat{\boldsymbol{q}}^{\mathrm{B}}) = \sum_{\nu}D^L_{\nu,M}(\boldsymbol{\beta})Y_{L\nu}(\hat{\boldsymbol{q}}^{\mathrm{lab}}), \quad (38)$$

$$Y^*_{LM}(\hat{\boldsymbol{q}}^{\mathrm{B}}) = \sum_{\nu}D^{L*}_{\nu,M}(\boldsymbol{\beta})Y^*_{L\nu}(\hat{\boldsymbol{q}}^{\mathrm{lab}}) \quad (39)$$

are utilized to transform $F^S_{f,i}(\Omega^{\mathrm{B}})$ to the laboratory-frame scattering amplitudes $F^S_{f,i}(\Omega^{\mathrm{lab}})$ via rotation by Euler angles $\boldsymbol{\beta}$, which orientate the body frame relative to the laboratory-frame [53,54]. The laboratory-frame scattering amplitudes are then obtained

$$F^S_{f,i}(\Omega^{\mathrm{lab}}) = (4\pi)^{-1/2}\sum_{\substack{L_f,L_i\\M_f,M_i}}\hat{L}_iF^{M\Pi S}_{fL_fM_f,iL_iM_i}D^{L_i*}_{0,M_i}(\boldsymbol{\beta}) \times\sum_{\nu}D^{L_f}_{\nu,M_f}(\boldsymbol{\beta})Y_{L_f\nu}\left(\hat{\boldsymbol{q}}_f^{\mathrm{lab}}\right), \quad (40)$$

where $\hat{\boldsymbol{q}}_f^{\mathrm{lab}}$ is the unit vector of the scattered electron, $\hat{L} = \sqrt{(2L+1)}$, and

$$F^{M\Pi S}_{fL_fM_f,iL_iM_i} = -(2\pi)^2(q_fq_i)^{-1}i^{L_i-L_f}e^{i(\sigma_{L_i}+\sigma_{L_f})} \times T^{M\Pi S}_{fL_fM_f,iL_iM_i}(q_f,q_i). \quad (41)$$

To save on computational resources and speed up convergence, an analytic Born subtraction technique is employed. This method relies on the property that for large values of orbital angular momentum, the partial-wave T-matrix elements are equal to the direct-potential partial-wave V matrix (first Born approximation)

$$T^{M\Pi S}_{fL_fM_f,iL_iM_i}(q_f,q_i) = \tilde{V}^{M\Pi}_{fL_fM_f,iL_iM_i}(q_f,q_i), \quad (42)$$

where q on the right-hand side refers to a plane wave and $\tilde{V}$ indicates the direct part of the interaction potential (27):

$$\tilde{V} = V_0 + \frac{Z_{\mathrm{ion}}}{r_0} + V_{01}. \quad (43)$$

Incorporating the analytic Born subtraction method for inelastic transitions, the laboratory-frame scattering amplitude

(40) is redefined as

$$F^{S}_{f,i}(\Omega^{\rm lab}) = \sum_{\substack{\lambda\mu \\ \lambda\mu}} F^{\rm AB}_{\substack{f,i \\ \lambda\mu}} \sum_{\rho} D^{\lambda *}_{\rho,\mu}(\boldsymbol{\beta}) Y^{*}_{\lambda\rho}(\hat{\boldsymbol{Q}}^{\rm lab}) + (4\pi)^{-1/2} \sum_{\substack{L_f,L_i \\ M_f,M_i}} \hat{L}_i \tilde{F}^{M\Pi S}_{fL_fM_f,iL_iM_i} D^{L_i *}_{0,M_i}(\boldsymbol{\beta}) \times \sum_{v} D^{L_f}_{v,M_f}(\boldsymbol{\beta}) Y_{L_f v}\left(\hat{\boldsymbol{q}}^{\rm lab}_f\right), \tag{44}$$

where

$$F^{\rm AB}_{\substack{f,i \\ \lambda\mu}} = -(2\pi)^2 i^{\lambda} V^{\rm AB}_{\substack{f,i \\ \lambda\mu}}(Q), \tag{45}$$

$$V^{\rm AB}_{\substack{f,i \\ \lambda\mu}}(Q) = -\frac{(-1)^{\lambda}\hat{\lambda}}{Q^2\pi^{3/2}} \sum_{\alpha\gamma} C^{(f)}_{\alpha} C^{(i)}_{\gamma} C^{l_\gamma 0}_{l_\alpha 0,\lambda 0} C^{l_\alpha m_\alpha}_{l_\gamma m_\gamma,\lambda\mu} \times \int_0^{\infty} dr_1 \varphi_\alpha(r_1) j_\lambda(Qr_1) \varphi_\gamma(r_1), \tag{46}$$

$\boldsymbol{Q} = \boldsymbol{q}_i - \boldsymbol{q}_f$, $j_\lambda(Qr_1)$ is a spherical Bessel function, and $C^{lm}_{l_1m_1,l_2m_2}$ denotes Clebsch-Gordan coefficients. In Eq. (44), $\tilde{F}^{M\Pi S}_{fL_fM_f,iL_iM_i}$ is defined as

$$\tilde{F}^{M\Pi S}_{fL_fM_f,iL_iM_i} = -(2\pi)^2 (q_f q_i)^{-1} i^{L_i - L_f} \times \left(e^{i(\sigma_{L_i}+\sigma_{L_f})} T^{M\Pi S}_{fL_fM_f,iL_iM_i}(q_f,q_i) - \tilde{V}^{M\Pi}_{fL_fM_f,iL_iM_i}(q_f,q_i)\right), \tag{47}$$

and $\tilde{V}^{M\Pi}_{fL_fM_f,iL_iM_i}(q_f,q_i)$ is from the partial-wave Born elements in (42).

Derivations of the adiabatic differential and integrated cross sections are found in Lane [55]. Here, we adopt a simpler but equivalent approach to obtain integrated cross sections. Averaging over all orientations of the molecule, the differential cross section (DCS) is defined as

$$\frac{d\sigma^{S}_{f,i}}{d\Omega^{\rm lab}} = \frac{q_f}{q_i}\left(\frac{1}{8\pi^2}\int \left|F^{S}_{f,i}(\Omega^{\rm lab})\right|^2 d\boldsymbol{\beta}\right). \tag{48}$$

Assuming the analytic Born subtraction method is not used, orientationally averaged partial-wave integrated cross sections are calculated via

$$\sigma^{M\Pi S}_{f,i} = \frac{q_f}{q_i}\frac{1}{4\pi} \sum_{\substack{L_f,L_i \\ M_f,M_i}} F^{M\Pi S}_{fL_fM_f,iL_iM_i} F^{M\Pi S *}_{fL_fM_f,iL_iM_i}. \tag{49}$$

The scattering amplitudes used in (49) can be expressed in terms of the the T-matrix elements or partial-wave Born elements $\tilde{V}^{M\Pi}_{fL_fM_f,iL_iM_i}(q_f,q_i)$. Using $\tilde{V}^{M\Pi}_{fL_fM_f,iL_iM_i}(q_f,q_i)$, the orientationally averaged partial-wave Born integrated cross sections $\sigma^{M\Pi}_{f,i}$ can be obtained. In this study, the Born subtraction method is utilized in the calculation of the orientationally averaged integrated cross sections

$$\sigma^{S}_{f,i} = \sum_{M\Pi}\left(\sigma^{M\Pi S}_{f,i} - \sigma^{M\Pi}_{f,i}\right) + \sigma^{\rm AB}_{f,i}, \tag{50}$$

where $\sigma^{\rm AB}_{f,i}$ are the orientationally averaged analytic Born integrated cross sections, which are calculated from the analytic Born DCS via numerical integration over $\hat{\boldsymbol{q}}^{\rm lab}_f$.

E. Adiabatic approximation: Vibrationally averaged cross sections

Following from Lane [55], orientationally averaged cross sections summed over all final rotational states J_f can be expressed in the form

$$\sigma^{S}_{fv_f,iv_i} = \frac{q_f}{q_i}\frac{1}{4\pi} \sum_{\substack{L_f,L_i \\ M_f,M_i}} \left|\langle \chi_{fv_f} \left| F^{S}_{fL_fM_f,iL_iM_i} \right| \chi_{iv_i} \rangle\right|^2, \tag{51}$$

where the vibrational wave functions $\chi_{nv}(R)$ are assumed to have no dependence on J. The above expression does not retain energy conservation, however, it is accurate outside the low-energy region [55]. Due to the completeness of the vibrational basis, the closure property

$$\sum_{v=0}^{N_B} \chi^{*}_{nv}(R')\chi_{nv}(R) + \int_0^{\infty} dk_v \chi_{nk_v}(R')\chi_{nk_v}(R) = \delta(R'-R) \tag{52}$$

is utilized to sum over all final vibrational state transitions to obtain

$$\sigma_{f,iv_i} = \sum_{v_f} \sigma_{fv_f,iv_i} = \int dR |\chi_{iv_i}(R)|^2 \sigma_{fi}(R), \tag{53}$$

where N_B is the highest bound vibrational state, σ_{f,iv_i} are cross sections resolved for an initial electronic, vibrational state transition to a final electronic state, and $\sigma_{fi}(R)$ are orientationally averaged cross sections calculated using Eq. (50). Expression (53) requires solution of the scattering problem at various internuclear distances and interpolation over R. To compare with experiment, cross sections need to be weighted to the bound H_2^+ vibrational levels via

$$\tilde{\sigma}_{f,i} = \sum_{v_i=0}^{N_v} p_{v_i} \sigma_{f,iv_i} \Bigg/ \left(\sum_{v_i=0}^{N_v} p_{v_i}\right), \tag{54}$$

where p_{v_i} are the Franck-Condon (FC) or von Busch and Dunn [15] (BD) distribution weights and N_v is the last vibrational state of the population.

III. RESULTS

A. Scattering calculation details

The electronic target structure of H_2^+ is calculated using the method described in Sec. II A. First, accurate $1s\sigma_g$ and $2p\sigma_u$ states were produced using a large Laguerre basis with $\alpha_l = 1.4$ basis functions with values of $l \leqslant 9$ and the number of functions $N_l = 60 - l$ taken to convergence (at the equilibrium distance of $R = 2.0$ and sufficiently accurate at $R = 5.5$). In the second step, the new Laguerre basis had the same values of exponential falloffs $\alpha_l = 1.4$ for basis functions with values of $l \leqslant 4$ and $N_l = 17 - l$. The $1s\sigma_g$ and $2p\sigma_u$ orbitals of this second basis were replaced with the accurate $1s\sigma_g$ and $2p\sigma_u$ states calculated at the first step. Omitting the highest-energy pseudostates, this diagonalization generated 351 states. The

TABLE I. Total energy of the electronic target states of H_2^+ are presented as a function of internuclear distances R for the states $1s\sigma_g$, $2p\sigma_u$, and $2p\pi_u$. Comparisons are made with the accurate calculations of Bates *et al.* [56]. All values are in atomic units.

	$1s\sigma_g$		$2p\sigma_u$		$2p\pi_u$	
R	CCC	[56]	CCC	[56]	CCC	[56]
0[a]	−2.000	−2.000	−0.500	−0.500	−0.500	−0.500
0.8	−0.304	−0.304	0.707	0.707	0.768	0.768
1.2	−0.528	−0.529	0.245	0.245	0.368	0.368
1.6	−0.590	−0.591	−0.008	−0.009	0.178	0.178
2.0	−0.601	−0.603	−0.166	−0.168	0.071	0.071
2.4	−0.594	−0.597	−0.270	−0.272	0.006	0.006
2.8	−0.581	−0.584	−0.339	−0.342	−0.037	−0.037
3.2	−0.567	−0.571	−0.386	−0.390	−0.066	−0.066
3.6	−0.553	−0.558	−0.417	−0.423	−0.086	−0.086
4.0	−0.540	−0.546	−0.439	−0.446	−0.100	−0.101
4.4	−0.528	−0.536	−0.453	−0.462	−0.110	−0.111
5.0	−0.513	−0.524	−0.466	−0.477	−0.120	−0.121
5.5	−0.503	−0.516	−0.472	−0.485	−0.125	−0.127

[a]This entry is the combined nuclear limit of H_2^+, which is He^+.

first few low-lying target state energies, oscillator strengths, and static dipole polarizability are presented as a function of R in Tables I, II, and III, respectively.

At large values of R, the single-center formulation requires large expansions to obtain accurate $1s\sigma_g$ and $2p\sigma_u$ state energies; other states are hydrogenic and are sufficiently accurate in the single-center formalism. For this reason, the ground-state nuclear wave functions $\Xi_{1v_J}(R)$ have been calculated using an accurate Born-Oppenheimer potential curve $\varepsilon_1(R)$ of H_2^+, which was provided by Wolniewicz and Poll [60] (private communication). Following the method in Sec. II A, this potential was diagonalized using a Laguerre basis with functions that have $J = 0$ and N_J taken to convergence.

TABLE II. 351-state oscillator strengths obtained in the length (L) and velocity (V) gauges are presented for transitions involving the $n = 1, 2$ levels of H_2^+ at various internuclear distances R. Results are compared with the accurate calculations of Bates [57], Bishop and Cheung [58], and Bates *et al.* [59]. All values are in atomic units.

	$1s\sigma_g \rightarrow 2p\sigma_u$			$1s\sigma_g \rightarrow 2p\pi_u$			$2p\sigma_u \rightarrow 2s\sigma_g$		
R	L	V	[57]	L	V	[58]	L	V	[59]
0	0.139	0.138		0.277	0.276				0
0.8	0.239	0.236	0.240	0.372	0.369	0.372	0.124	0.121	0.124
1.2	0.293	0.288	0.292	0.412	0.409	0.412	0.156	0.155	0.156
1.6	0.317	0.310	0.317	0.441	0.437	0.441	0.152	0.153	0.152
2.0	0.320	0.311	0.319	0.461	0.456	0.460	0.137	0.139	0.136
2.4	0.310	0.301	0.310	0.473	0.467	0.472	0.121	0.123	
2.8	0.295	0.287	0.297	0.479	0.472	0.478	0.108	0.110	
3.2	0.277	0.269	0.281	0.480	0.471	0.478	0.097	0.099	
3.6	0.256	0.250	0.261	0.476	0.465	0.473	0.085	0.086	
4.0	0.234	0.231	0.238	0.469	0.455	0.465	0.066	0.067	0.081
4.4	0.210	0.211	0.213	0.458	0.441		0.023	0.026	
5.0	0.172	0.183	0.175	0.436	0.414	0.430	0.035	0.017	0.077
5.5	0.140	0.162	0.144	0.415	0.388		0.057	0.027	

TABLE III. Static dipole polarizability of the H_2^+ ground state resulting from the 351-state diagonalization is presented as a function of internuclear distance R. Comparing with the accurate calculations of Bishop and Cheung [58]. All values are in atomic units. The number in parentheses indicates that the entry is multiplied by 10 to the power of the number in parentheses.

	$\alpha_\parallel$		$\alpha_\perp$	
R	CCC	[58]	CCC	[58]
0	0.2812(0)		0.2812(0)	
0.8	0.8105(0)	0.8096(0)	0.6293(0)	0.6283(0)
1.2	0.1540(1)	0.1538(1)	0.9446(0)	0.9426(0)
1.6	0.2842(1)	0.2837(1)	0.1328(1)	0.1324(1)
2.0	0.5084(1)	0.5078(1)	0.1767(1)	0.1758(1)
2.4	0.8865(1)	0.8860(1)	0.2240(1)	0.2224(1)
2.8	0.1514(2)	0.1515(2)	0.2731(1)	0.2701(1)
3.2	0.2545(2)	0.2552(2)	0.3212(1)	0.3165(1)
3.6	0.4228(2)	0.4248(2)	0.3663(1)	0.3593(1)
4.0	0.6948(2)	0.7005(2)	0.4075(1)	0.3964(1)
4.4	0.1136(3)		0.4424(1)	
5.0	0.2364(3)	0.2375(3)	0.4821(1)	0.4579(1)
5.5	0.4390(3)		0.5035(1)	

Previous investigation [34] found that weighting cross sections across all bound vibrational states is important. Molecular state energies and Franck-Condon (FC) factors

$$\mathrm{FC}_{f v_f J_f, i v_i J_i} = \left| \int d\boldsymbol{R}\, \Xi^*_{f v_f J_f}(\boldsymbol{R}) \Xi_{i v_i J_i}(\boldsymbol{R}) \right|^2, \qquad (55)$$

for the single-ionization transition between the neutral molecule and its ion are presented in Tables IV for H_2^+, V for D_2^+, and VI for T_2^+. A plot of the FC factors is given in Fig. 1. The FC factors calculated here are used to weight cross sections according to Eq. (54). The Born-Oppenheimer potential energy curve of $H_2(X\,^1\Sigma_g)$ was taken from Kolos *et al.* [61].

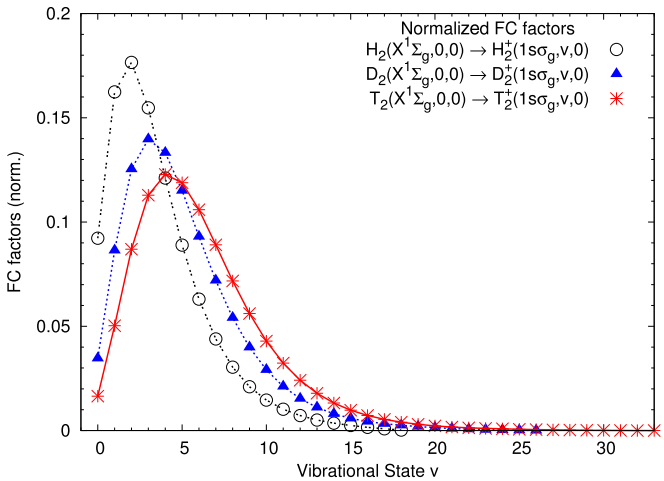

FIG. 1. (Color online) Normalized Franck-Condon (FC) factors of $H_2(X\,^1\Sigma_g,0,0) \rightarrow H_2^+(1s\sigma_g,v,0)$, $D_2(X\,^1\Sigma_g,0,0) \rightarrow D_2^+(1s\sigma_g,v,0)$ and $T_2(X\,^1\Sigma_g,0,0) \rightarrow T_2^+(1s\sigma_g,v,0)$.

TABLE IV. Born-Oppenheimer molecular state energy levels of $H_2^+(1s\sigma_g,v,0)$. Franck-Condon (FC) factors and von Busch and Dunn [15] (BD) weights are given for the transition $H_2(X\,^1\Sigma_g,0,0) \rightarrow H_2^+(1s\sigma_g,v,0)$. Results are compared with the calculations of Wünderlich and Fantz [62]. The asterisk denotes "stated as unbound by potential energy curve."

	Energy (eV)		Weighting		
v	Present	[62]	Present FC	FC [62]	BD [15]
0	−16.25594	−16.25498	0.0909007	0.0911850	0.11916
1	−15.98416	−15.98338	0.1600668	0.1605800	0.18994
2	−15.72816	−15.72753	0.1739719	0.1742600	0.18791
3	−15.48744	−15.48685	0.1525290	0.1521300	0.15173
4	−15.26153	−15.26086	0.1193440	0.1190800	0.11097
5	−15.05009	−15.04958	0.0876249	0.0875530	0.07732
6	−14.85282	−14.85237	0.0621211	0.0619910	0.05270
7	−14.66951	−14.66909	0.0432688	0.0431950	0.03564
8	−14.50006	−14.49974	0.0299371	0.0299210	0.02411
9	−14.34441	−14.34421	0.0207168	0.0207080	0.01638
10	−14.20260	−14.20250	0.0143968	0.0143850	0.01121
11	−14.07479	−14.07476	0.0100634	0.0100560	0.00773
12	−13.96122	−13.96126	0.0070698	0.0070679	0.00536
13	−13.86222	−13.86239	0.0049739	0.0049789	0.00374
14	−13.77832	−13.77860	0.0034781	0.0034841	0.00258
15	−13.71018	−13.71057	0.0023777	0.0023826	0.00175
16	−13.65863	−13.65909	0.0015287	0.0015298	0.00109
17	−13.62460	−13.62566	0.0008294	0.0007257	0.00056
18	−13.60854	*	0.0002434	*	0.00012

To demonstrate the accuracy of the molecular convergent close-coupling (CCC) code, calculations have been performed in the unified atom limit ($R = 0$) for H_2^+, which equivalently is the He^+ ion. The molecular CCC code calculations used the same Laguerre basis as the atomic CCC code [63], which produced convergent results. Figure 2 presents total ionization cross sections of electron scattering from the ground state of He^+ using a 289-state molecular CCC code calculation.

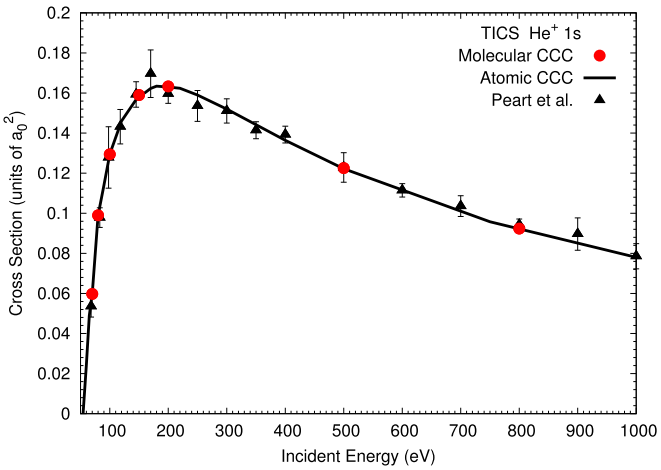

FIG. 2. (Color online) Total ionization cross sections (TICS) of electron scattering from the electronic ground state of He^+. The molecular CCC united atom ($R = 0\ a_0$) calculations are compared with the atomic CCC code calculations [63] and the measurements of Peart *et al.* [64].

These results are compared with the atomic CCC code calculations [63] and the experimental measurements of Peart *et al.* [64]. The two codes are in excellent agreement with each other and experiment across the entire energy range.

351-state CCC calculations were conducted over the energy range from 10 to 1000 eV. Calculations were performed with partial waves up to the total angular projection $M = 9$, orbital angular momentum $L = 9$, singlet and triplet spin S, and odd and even parity Π. An orientationally averaged analytic Born subtraction method (described in Sec. II D) was used to top up the partial-wave expansion. Convergence of the 351-state calculation is demonstrated by comparing with the results of a 289-state calculation at a fixed-nuclear distance of $R = 2.0$. The 289 states used in the calculation were generated from the two-step diagonalization method described in Sec. II A.

TABLE V. Born-Oppenheimer molecular state energy levels of $D_2^+(1s\sigma_g,v,0)$. Franck-Condon (FC) factors are given for the transition $D_2(X\,^1\Sigma_g,0,0) \rightarrow D_2^+(1s\sigma_g,v,0)$. Results are compared with the calculations of Wünderlich and Fantz [62]. The asterisk denotes "stated as unbound by potential energy curve."

	Energy (eV)		Weighting			Energy (eV)		Weighting	
v	Present	[62]	Present FC	FC [62]	v	Present	[62]	Present FC	FC [62]
0	−16.29734	−16.29634	0.0344701	0.0346030	14	−14.23559	−14.23575	0.0080059	0.0080244
1	−16.10177	−16.10084	0.0859598	0.0863810	15	−14.14066	−14.14152	0.0058199	0.0058630
2	−15.91421	−15.91357	0.1247462	0.1251600	16	−14.05241	−14.05432	0.0043019	0.0043087
3	−15.73448	−15.73368	0.1390024	0.1387300	17	−13.97120	−13.97429	0.0032599	0.0031850
4	−15.56240	−15.56166	0.1325658	0.1325300	18	−13.89749	−13.90154	0.0024991	
5	−15.39779	−15.39701	0.1144811	0.1141200	19	−13.83148	−13.83622	0.0018842	
6	−15.24052	−15.23974	0.0925865	0.0924670	20	−13.77324	−13.77855	0.0013713	
7	−15.09046	−15.08978	0.0716467	0.0715630	21	−13.72300	−13.72875	0.0009640	
8	−14.94752	−14.94684	0.0538533	0.0537870	22	−13.68126	−13.68711	0.0006583	
9	−14.81160	−14.81097	0.0397230	0.0397380	23	−13.64857	−13.65394	0.0004321	
10	−14.68264	−14.68209	0.0289739	0.0289910	24	−13.62536	−13.62969	0.0002588	
11	−14.56060	−14.56013	0.0210232	0.0210130	25	−13.61170	*	0.0001202	*
12	−14.44543	−14.44507	0.0152415	0.0152160	26	−13.60659	*	0.0000265	*
13	−14.33713	−14.33695	0.0110512	0.0110340					

TABLE VI. Born-Oppenheimer molecular state energy levels of $T_2{}^+(1s\sigma_g,v,0)$. Franck-Condon (FC) factors are given for the transition $T_2(X\,{}^1\Sigma_g,0,0) \rightarrow T_2{}^+(1s\sigma_g,v,0)$. Results are compared with the calculations of Wünderlich and Fantz [62]. The asterisk denotes "stated as unbound by potential energy curve."

	Energy (eV)		Weighting			Energy (eV)		Weighting	
v	Present	[62]	Present FC	FC [62]	v	Present	[62]	Present FC	FC [62]
0	−16.31572	−16.31470	0.0164282	0.0164670	17	−14.25558	−14.25539	0.0053657	0.0053434
1	−16.15469	−16.15369	0.0501630	0.0505410	18	−14.17672	−14.17672	0.0039946	
2	−15.99905	−15.99841	0.0867873	0.0871240	19	−14.10236	−14.10273	0.0029681	
3	−15.84869	−15.84784	0.1126303	0.1126800	20	−14.03241	−14.03347	0.0022145	
4	−15.70352	−15.70281	0.1225468	0.1223600	21	−13.96697	−13.96903	0.0016841	
5	−15.56342	−15.56257	0.1185671	0.1183400	22	−13.90637	−13.90944	0.0013151	
6	−15.42833	−15.42754	0.1056883	0.1055500	23	−13.85092	−13.85479	0.0010416	
7	−15.29814	−15.29732	0.0888531	0.0886560	24	−13.80080	−13.80521	0.0008156	
8	−15.17280	−15.17202	0.0716072	0.0715640	25	−13.75603	−13.76082	0.0006189	
9	−15.05225	−15.05152	0.0559802	0.0559270	26	−13.71668	−13.72173	0.0004539	
10	−14.93643	−14.93571	0.0428184	0.0428000	27	−13.68299	−13.68815	0.0003240	
11	−14.82530	−14.82462	0.0322589	0.0322840	28	−13.65526	−13.66020	0.0002255	
12	−14.71883	−14.71819	0.0240594	0.0240790	29	−13.63378	−13.63809	0.0001502	
13	−14.61699	−14.61638	0.0178323	0.0178500	30	−13.61870	−13.62273	0.0000906	
14	−14.51976	−14.51920	0.0131779	0.0131970	31	−13.60993	*	0.0000424	*
15	−14.42711	−14.42665	0.0097356	0.0097472	32	−13.60652	*	0.0000110	*
16	−14.33904	−14.33871	0.0072128	0.0072057	33	−13.60573	*	0.0000035	*

The second basis had functions with exponential falloffs $\alpha_l = 1.4$, values of $l \leqslant 4$ and $N_l = 15 - l$. In Fig. 3, we compare the proton production (PP) and dissociative ionization (DI) cross sections resulting from the 351-state and 289-state calculations. Results from the two calculations indicate that they are converged. The PP cross section feature at 20 eV is from the newly opened $2p\pi_u$ states contribution to the cross section.

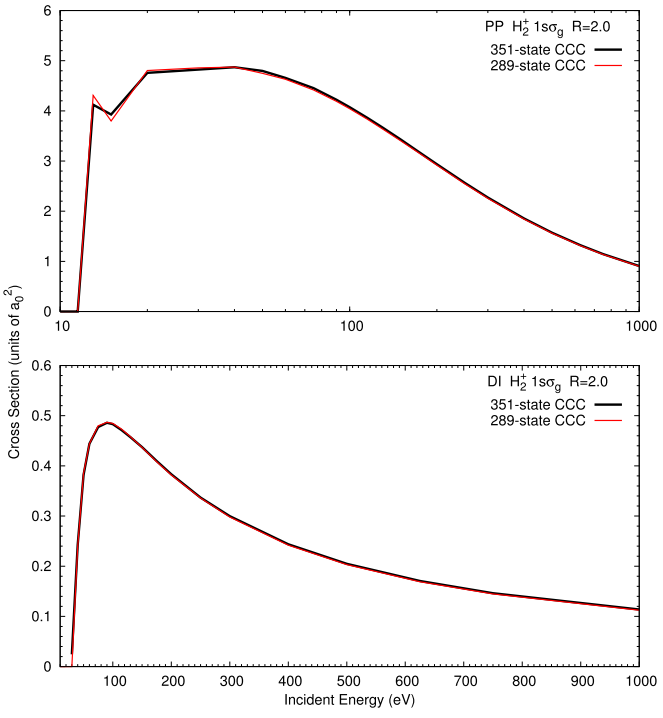

FIG. 3. (Color online) 351- and 289-state CCC results of proton production (PP) and dissociative ionization (DI) cross sections of electron scattering from $H_2{}^+$ at a fixed-nuclear distance of $R = 2.0\,a_0$.

351-state scattering calculations were conducted over a 23-point R grid within the interval $1.2 \leqslant R \leqslant 5.5$. Resulting $\sigma_{PP}(R)$ and $\sigma_{DI}(R)$ were found to be smooth with respect to the internuclear distance R. These cross sections were interpolated and extrapolated across the grid $1.0 \leqslant R \leqslant 18.0$, the span of the highest excited vibrational levels. Extrapolation outside the interval $1.2 \leqslant R \leqslant 5.5$ introduces uncertainty in the vibrationally weighted cross sections. By investigating different extrapolation techniques, the resulting vibrationally weighted cross sections were found to be quite stable. As an additional check, vibrationally weighted analytic Born cross sections were calculated using the same method described above. The resulting vibrationally weighted analytic Born cross sections compared very well with the results of Peek and Green [21] (constructed from Table I in [21]). Vibrationally resolved analytic Born cross sections also compared well with Peek and Green [21]. It is estimated that the vibrationally weighted CCC cross sections have a maximum error of 5% from the extrapolation.

Results are not presented for impact energies below 10 eV. This region has significant indirect processes [2] which are unaccounted for and the closure approximation breaks down near respective transition thresholds (in this case for the dominant dissociative excitation transition $1s\sigma_g, v_i \rightarrow 2p\sigma_u$).

Many applications of collision data require an estimate of the associated uncertainty in the final cross sections. Here, we estimate that convergence of the close-coupling and partial-wave expansions have each been achieved to less than 5% accuracy. Uncertainty associated with extrapolation to larger internuclear distances R is estimated to be less than 5% and the error associated with the adiabatic closure approximation is estimated to be less than 1% [21]. We estimate that the accuracy

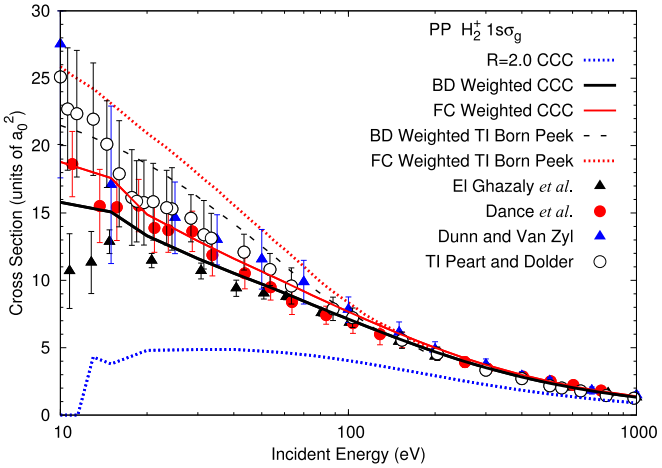

FIG. 4. (Color online) Franck-Condon (FC) and von Busch and Dunn [15] (BD) vibrationally weighted proton production (PP) cross sections for electron scattering from the electronic ground, vibrationally excited states of H_2^+. Results are compared with the present $R = 2.0\,a_0$ calculations, vibrationally weighted total inelastic (TI) Born calculations of Peek [20], the TI measurements of Peart and Dolder [8], and the PP experiments of El Ghazaly *et al.* [7], Dunn *et al.* [3,4], and Dance *et al.* [5].

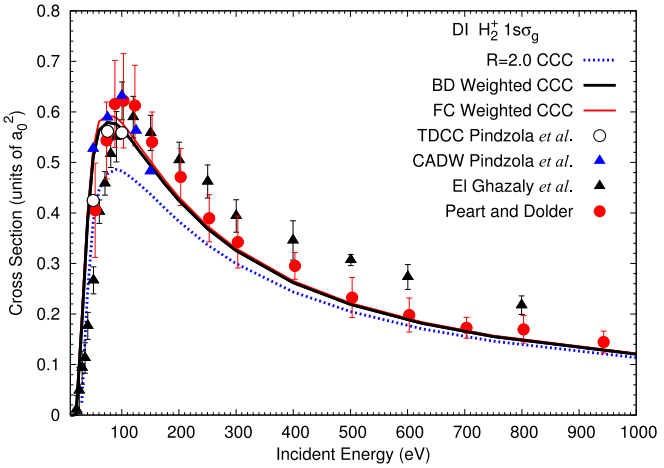

FIG. 5. (Color online) Franck-Condon (FC) and von Busch and Dunn [15] (BD) vibrationally weighted dissociative ionization (DI) cross sections for electron scattering from the electronic ground, vibrationally excited states of H_2^+. Results are compared with the present $R = 2.0\ a_0$ results, the $R = 2.0\ a_0$ configuration-average distorted-wave (CADW) method [33], the $R = 2.0\,a_0$ time-dependent close-coupling (TDCC) method [32], and measurements of Peart and Dolder [14] and El Ghazaly *et al.* [7].

of DI (less than 5%) is higher than PP (less than 10%). This is due to PP having a higher sensitivity to extrapolation.

B. H_2^+

The 351-state adiabatic CCC results of vibrationally weighted PP cross sections are presented in Fig. 4 for electron scattering from H_2^+. These results are compared with the present fixed-nuclei calculations at $R = 2.0$, vibrationally weighted total inelastic (TI) Born cross sections of Peek [20], the TI measurements of Peart and Dolder [8], and the PP measurements of El Ghazaly *et al.* [7], Dunn *et al.* [3,4], and Dance *et al.* [5]. Note again that the TI and PP cross sections can be readily compared with each other (referring to Sec. I). The difference between previous results [34] and results presented here come from the improved accuracy of the $2p\sigma_u$ state. Here, the difference in results using the von Busch and Dunn [15] (BD) and FC distribution is only seen in the low-energy region (10–20 eV), where vibrational dependence is extremely important (in particular for the high-lying vibrational levels). FC weighting leads to a larger cross section due to their slightly heavier weighting on the highly excited vibrational states. Again, the $R = 2.0$ results structure at 20 eV is from the newly opened $2p\pi_u$ states' contribution to the cross section. Comparing the $R = 2.0$ and vibrationally weighted cross sections, the importance of accounting for the vibrational distribution of H_2^+ is evident, where the vibrationally weighted cross sections are about 380% larger at lower energies. In the low- and intermediate-energy (20–100 eV) regions, the vibrationally weighted cross sections are in good agreement with the experiments of Dance *et al.* [5] and Peart and Dolder [8]. The large variation in experimental data in the low-energy region could be due to the production of different vibrational populations of H_2^+, where the dissociative excitation (DE) cross sections are highly dependent upon the initial vibrational state of H_2^+. Peart and Dolder [8] have also outlined some other possible reasons for this variation in experimental data. It should be noted again that the experiments of Peart and Dolder [8] and Dunn *et al.* [3,4] were designed to produce H_2^+ ions in a vibrational population given by the FC factors. El Ghazaly *et al.* [7] stated that their measurements indicated that their H_2^+ ions were not produced in the $v \geqslant 14$ states. This could be the reason for the discrepancy in the low-energy region. In the high-energy region (100–1000 eV), the CCC results are in good agreement with all experiments and the vibrationally weighted Born cross sections of Peek [20].

DI cross sections of electron scattering from vibrationally excited H_2^+ are presented in Fig. 5. The vibrationally weighted 351-state CCC results are compared with the present fixed-nuclei $R = 2.0$ results, the fixed-nuclei $R = 2.0$ time-dependent close-coupling (TDCC) [32], and $R = 2.0$ configuration-average distorted-wave (CADW) [33] results, and the measurements of Peart and Dolder [14] and El Ghazaly *et al.* [7]. Comparing the $R = 2.0$ calculations, the CCC DI cross sections are lower than the TDCC results; at the peak of the cross section (75 eV), the difference is about 20%. The CADW [33] results are higher than the TDCC and CCC results at the cross-section peak; this is expected low-energy behavior for a first-order method. The present fixed-nuclei results are about 20% lower than the vibrationally weighted results. FC and BD weighted DI cross sections are in excellent agreement with the measurements of Peart and Dolder [14], however, they do not agree with the most recent measurements of El Ghazaly *et al.* [7]. The experiment conducted by El Ghazaly *et al.* [7] differentiated protons resulting from DI or DE by analyzing the kinetic energy release spectrum of the ions. In their analysis, they assumed that the DI cross sections are not dependent upon R and, hence, $\sigma_{\mathrm{DI}}(R)$ is constant. This allowed them to

distinguish DI by extracting the DI cross section from the tail of the kinetic energy release spectrum. El Ghazaly *et al.* [7] expected that such a procedure would produce inaccurate results only for lower energies, however, the disagreement between CCC results persists to high energies. Results from the current calculations show a linear growing $\sigma_{\rm DI}(R)$ dependence with R. For single-photon ionization of $H_2{}^+$, Chapman [65] reported cross sections with a significant dependence on R. The excellent agreement between the vibrationally weighted CCC results and the experiment of Peart and Dolder [14] is most encouraging considering the fact that they differentiated the DI cross section from the DE cross section by measuring protons arriving at detectors in coincidence.

Further investigation identified the difference between the fixed-nuclei $R = 2.0$ CCC and TDCC DI cross sections. As demonstrated, the CCC results are converged, smooth, and were produced with an accurate $H_2{}^+$ structure. We have achieved convergence in the partial-wave expansion of the projectile ($L = 9$ and $M = 9$) with analytic Born subtraction or distorted-wave top-up for the higher terms. The TDCC results [32] were calculated with the partial-wave expansion $L = 5$ and $M = 2$ with distorted-wave top-up for the higher terms. CCC calculations with the same partial-wave expansion as in the TDCC calculations resulted in DI cross sections that are 15% larger, and in good agreement with the TDCC results. This suggests that the larger partial-wave expansion is required for greater accuracy.

The present adiabatic CCC results can be used to obtain electron scattering cross sections that are resolved for vibrationally excited states of $H_2{}^+$. DE and DI cross sections are presented as a function of the molecule's initial vibrational state v_i in Fig. 6. Cross sections are presented up to the vibrational state $v_i = 9$, which spans over the range $1.0 \leqslant R \leqslant 5.5$. The DE and DI cross sections have a major dependence on v_i at the cross-section maximum and in the intermediate-energy region. There is also a significant dependence on v_i at higher energies. For example, the $v_i = 9$ DI cross section at 750 eV is 30% larger than the $v_i = 0$ cross section. Both the DE and DI cross sections monotonically increase across the entire

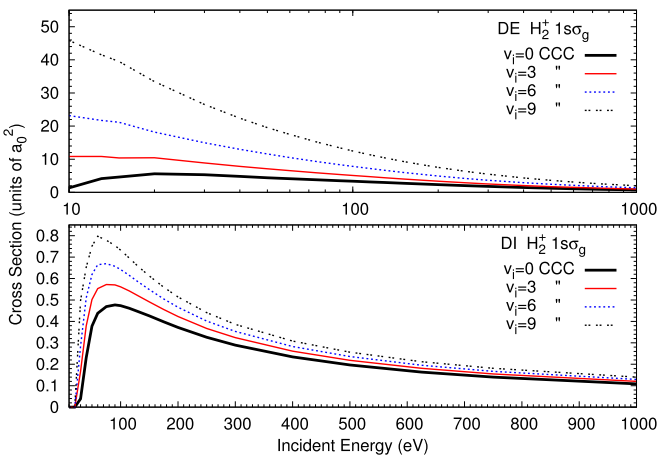

FIG. 6. (Color online) Dissociative excitation (DE) and dissociative ionization (DI) cross sections for electron scattering from $H_2{}^+$ in the electronic ground, vibrational state v_i.

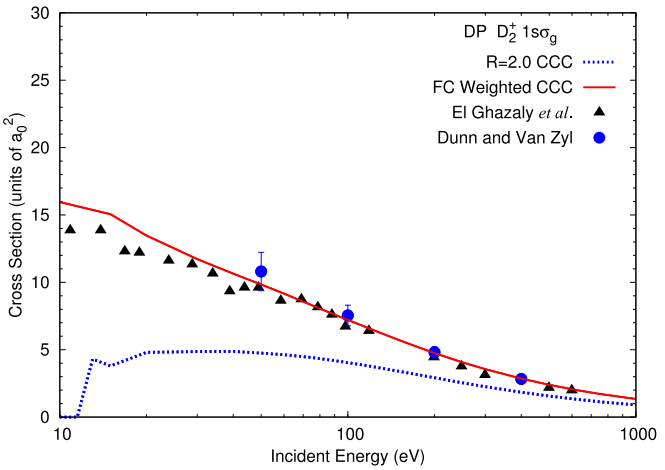

FIG. 7. (Color online) Franck-Condon (FC) weighted deuteron production (DP) cross sections for electron scattering from the electronic ground, vibrationally excited states of $D_2{}^+$. Results are compared with the experiments of El Ghazaly *et al.* [7] and Dunn and Van Zyl [4].

energy range as v_i increases and the cross-section peak shifts to lower energies. Looking at the $v_i = 9$ DI cross-section peak (60 eV), this cross section is about 70% larger than the $v_i = 0$ cross-section peak (at 90 eV). For DE, comparing the cross sections at 20 eV for the $v_i = 9$ and $v_i = 0$ states, the $v_i = 9$ state cross section is 500% larger than the $v_i = 0$ state. While at 750 eV the DE cross section of the $v_i = 9$ state is about 180% larger than the $v_i = 0$ state. This behavior of the present DE cross sections is consistent with the conclusions drawn by Peek [16,19]. The monotonic increase and cross-section peak shift of DE and DI processes comes from lower excitation and ionization thresholds as R increases. Also, as R increases, more electronic dissociative states rise and enter into the ionization continuum, increasing the DI cross section.

C. $D_2{}^+$

Using vibrational wave functions of $D_2{}^+$ in Eq. (53), adiabatic CCC results are obtained for electron scattering from $D_2{}^+$. In Fig. 7, vibrationally weighted deuteron production (DP) cross sections are presented for electron scattering from vibrationally excited $D_2{}^+$. The vibrationally weighted CCC results are compared with the measurements of El Ghazaly *et al.* [7] and Dunn and Van Zyl [4]. In the high- and intermediate-energy regions, the CCC results are in excellent agreement with both experiments. Results in the low-energy region overestimate the measurements of El Ghazaly *et al.* [7] by about 15%. DE cross sections in the low-energy region are highly sensitive to the vibrational population, hence, this discrepancy could be due to the different vibrational population assumed here and that which was produced in experiment. Measurements of $H_2{}^+$ and $D_2{}^+$ are within the error bars of each other and hence fail to show any isotopic affects. CCC results have a minor difference in the low-energy region as a result of isotopic effects; this will be discussed further in the following section.

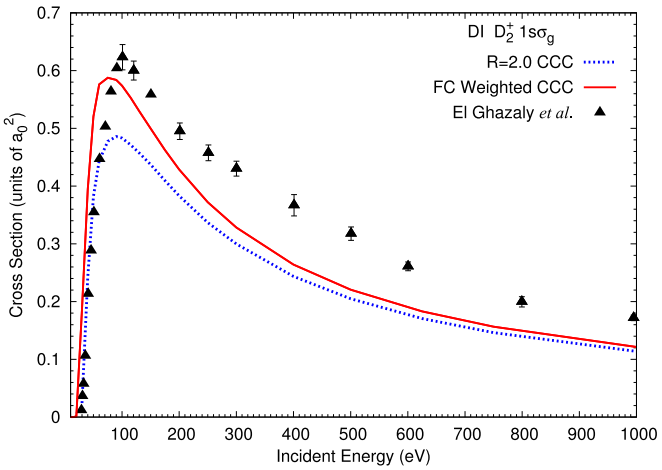

FIG. 8. (Color online) Franck-Condon (FC) weighted dissociative ionization (DI) cross sections for electron scattering from the electronic ground, vibrationally excited states of D_2^+. Results are compared with the experiment of El Ghazaly *et al.* [7].

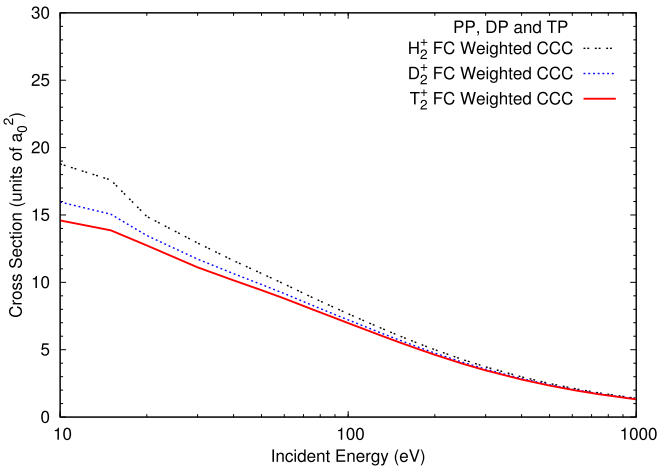

FIG. 10. (Color online) Proton production (PP), deuteron production (DP), and triton production (TP) cross sections for electron scattering from vibrationally excited H_2^+, D_2^+, or T_2^+, respectively. Vibrational cross sections are weighted according to the Franck-Condon (FC) factors.

Vibrationally weighted DI cross sections are plotted in Fig. 8 for D_2^+. The adiabatic CCC results are presented alongside the measurements of El Ghazaly *et al.* [7]. First, the vibrationally weighted CCC results of D_2^+ are within 1% of the FC weighted results of H_2^+. Again, the vibrationally weighted CCC results do not agree with the measurements of El Ghazaly *et al.* [7]. Reasons for this disagreement are the same for H_2^+ and have been discussed in the previous section.

Our calculations allow for DE and DI cross sections to be resolved for electron scattering from D_2^+ in a vibrationally excited state v_i. The DE and DI cross sections are presented up to $v_i = 13$ in Fig. 9. The D_2^+ $v_i = 13$ state spans the range $1.0 \leqslant R \leqslant 5.5$. Like H_2^+, DE and DI cross sections are highly dependent on the initial vibrational state of the molecule. Major dependence is seen at the peak of the cross section and in the intermediate-energy region, while in the high-energy region, cross sections significantly depend on the initial vibrational state of the molecule. As an indication, the $v_i = 13$ DI cross-section peak (at 60 eV) is 70% larger than the $v_i = 0$ cross-section peak (at 90 eV). The cross sections also increase monotonically across all energies as v_i increases. Comparing vibrationally resolved DE and DI cross sections of H_2^+ and D_2^+, there is little difference when the respective molecule's vibrational state spans the same range of R. For example, the $v_i = 13$ DI cross-section peak of D_2^+ is practically the same as the H_2^+ $v_i = 9$ (also spans the range $1.0 \leqslant R \leqslant 5.5$) cross-section peak (also at 60 eV). The major difference in the cross section is seen near the respective threshold, however, this where the closure method is inaccurate.

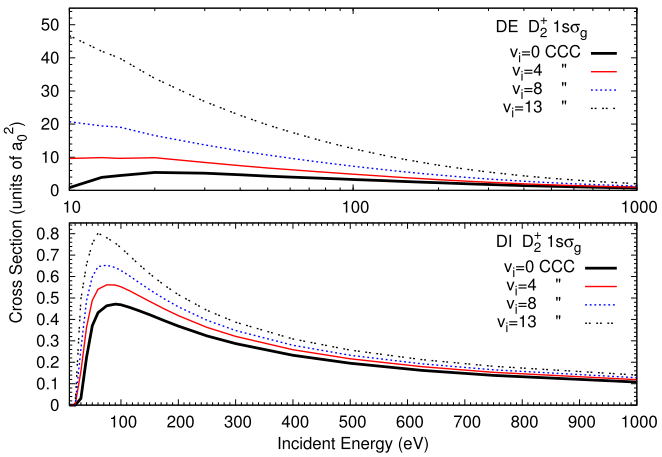

FIG. 9. (Color online) Dissociative excitation (DE) and dissociative ionization (DI) cross sections for electron scattering from D_2^+ in the electronic ground, vibrational state v_i.

D. T_2^+

In Fig. 10, the vibrationally weighted triton production (TP) cross sections are presented. These are compared with the FC weighted PP cross sections of H_2^+ and DP cross sections of D_2^+. Little difference in the cross sections are seen in the high- and intermediate-energy regions. In the low-energy region, isotopic affects are evident. Experimentally, these molecular ions are produced from their corresponding neutral molecule, i.e., $H_2(X\,^1\Sigma_g,0,0) \rightarrow H_2^+(1s\sigma_g,v,0)$. The lightest neutral molecule H_2 has a more diffuse vibrational ground-state wave function that reaches smaller and larger values of R compared to its heavier isotopologues D_2 and T_2. This results in lighter molecular ions having slightly heavier FC weighting on highly excited vibrational states. From Eqs. (53) and (54), we note that the larger weighting on highly excited vibrational states that span large values of R allow significant contribution of $\sigma_{f,i}(R)$ at large values of R. At these large values of R, the DE cross section is very large due to the decreasing threshold of the $2p\sigma_u$ state. These differences in vibrational populations are responsible for the variation of low-energy cross sections and lead to isotopic effects.

The individual cross-section contributions from the FC weighted vibrational states are given in Figs. 11 and 12 for H_2^+, D_2^+, and T_2^+. PP, DP, and TP cross sections are given

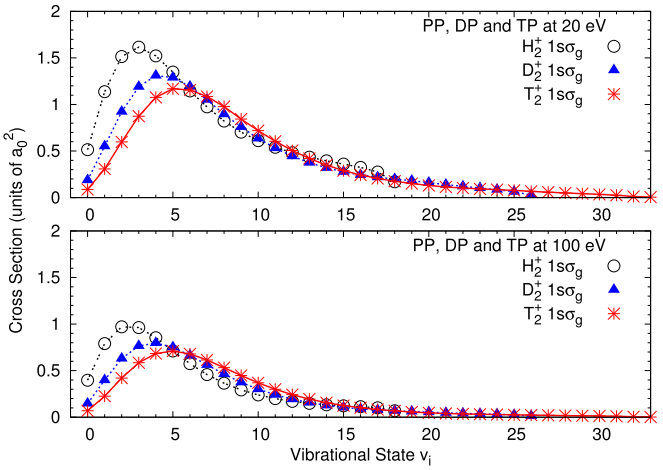

FIG. 11. (Color online) Proton production (PP), deuteron production (DP), and triton production (TP) cross sections for 20 and 100 eV electron scattering from H_2^+, D_2^+, or T_2^+, respectively. The molecular ions are in the electronic ground, vibrational state v_i. Cross sections are weighted according to their Franck-Condon factors.

for the impact energies 20 and 100 eV. At these energies, the weighted cross sections come predominantly from the ground and first few vibrationally excited states. This trend follows the respective molecule's FC distribution as seen in Fig. 1, however, at the impact energy of 20 eV, the highly excited vibrational states contribute more than the FC trend shows. This is due to the vibrationally excited states very large DE cross sections in the low-energy region, which are a result of the decrease in excitation threshold. The FC DI cross sections at an impact energy of 100 eV are almost identical to the FC factors trend. DI cross sections are not as sensitive to the initial vibrational state of the molecule compared to the DE cross sections. This is consistent with the behavior of the static dipole polarizibility contribution from the DE and ionization continuum states as a function of R. Analyzing our

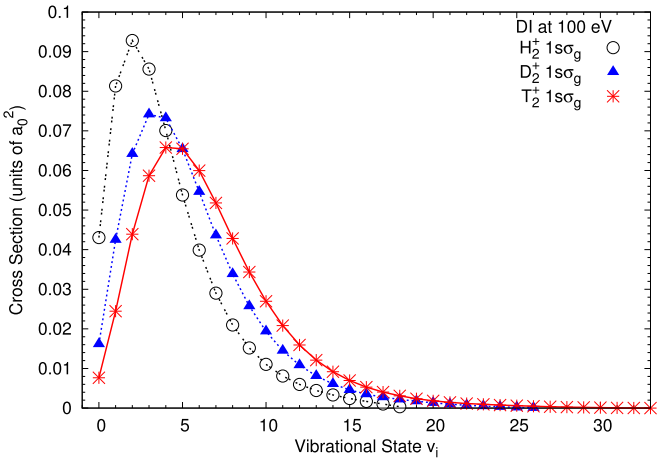

FIG. 12. (Color online) Dissociative ionization (DI) cross sections for 100 eV electron's scattering from H_2^+, D_2^+, or T_2^+, respectively. The molecular ions are in the electronic ground, vibrational state v_i. Cross sections are weighted according to their Franck-Condon factors.

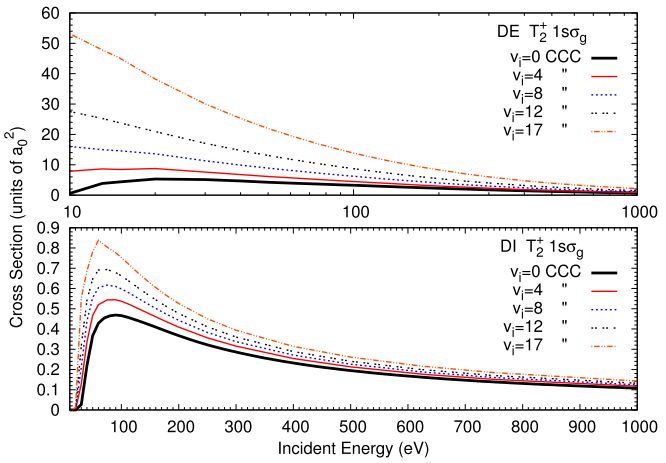

FIG. 13. (Color online) Dissociative excitation (DE) and dissociative ionization (DI) cross sections for electron scattering from T_2^+ in the electronic ground, vibrational state v_i.

calculations of polarizability for H_2^+, the contribution from DE states increases rapidly with R and is much larger than the contribution from continuum states. Hence, the DE cross sections are expected to be more sensitive to increases in R than the DI cross sections.

Vibrationally resolved DE and DI cross sections of T_2^+ are given up to $v_i = 17$ (approximately spans the range $1.0 \leqslant R \leqslant 5.5$) in Fig. 13. Much like H_2^+ and D_2^+, the DE and DI cross sections are highly dependent upon the initial vibrational state of the molecule.

E. HD^+

Unlike the homonuclear molecular ions H_2^+, D_2^+, and T_2^+, all heterogeneous molecular ions HD^+, HT^+, and DT^+ have a permanent electric dipole moment and internally cool via rotational-vibrational radiative transitions. This allows the preparation of HD^+, HT^+, and DT^+ in the ground $v = 0$ vibrational state. For this reason, averaging over the vibrational distribution is not required and we do not present FC weighted cross sections for HD^+, HT^+, and DT^+.

DE cross sections are presented in the top panel Fig. 14 for electron scattering from HD^+ in the vibrationally excited state v_i. From here onwards, cross sections presented as a function of v_i will only be presented up to the vibrational state that spans the range $1.0 \leqslant R \leqslant 5.5$. The $v_i = 0$ DE cross sections are compared with the experiment of Andersen *et al.* [13]. The adiabatic CCC results are in excellent agreement with experiment after the $2p\sigma_u$ threshold. Noting that the current formulation neglects the indirect (resonant) channels, this agreement with experiment above the $2p\sigma_u$ threshold indicates the dominance of the direct-scattering process. These conclusions are consistent with those of Fifirig and Stroe [2].

The bottom panel of Fig. 14 is a plot of the DI cross sections of HD^+ as a function of its initial vibrational state. Cross sections are presented up to the state $v_i = 11$. Again, the cross sections characteristics are affected by v_i in the same way as the other isotopologues. The difference between the isotopologues

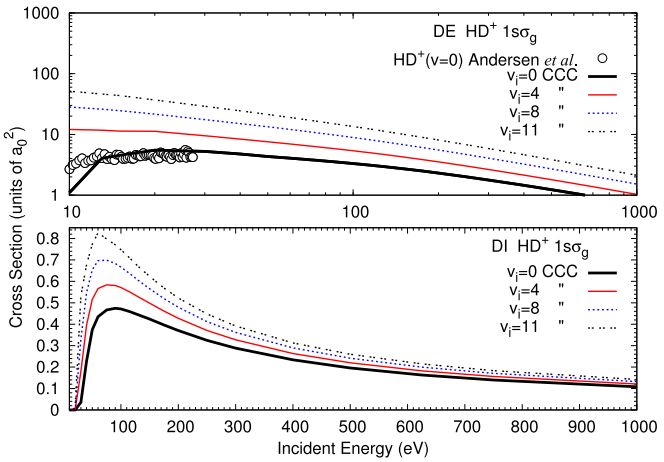

FIG. 14. (Color online) Dissociative excitation (DE) and dissociative ionization (DI) cross sections for electron scattering from HD^+ in the electronic ground, vibrational state v_i. DE results of HD^+ in the vibrational ground state are compared with the experiment of Andersen *et al.* [13].

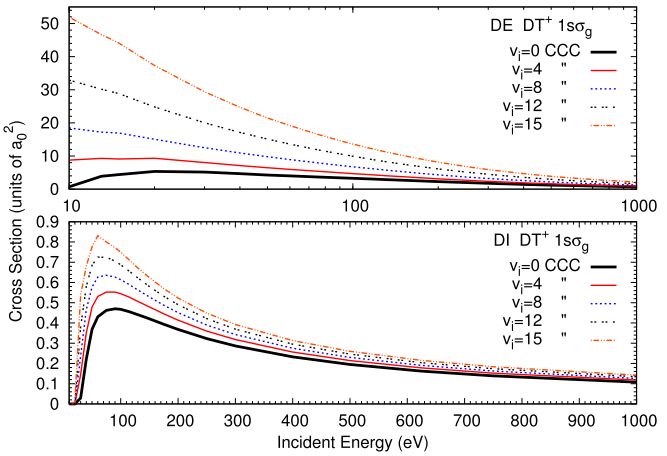

FIG. 16. (Color online) Dissociative excitation (DE) and dissociative ionization (DI) cross sections for electron scattering from DT^+ in the electronic ground, vibrational state v_i.

vibrationally resolved cross sections is just the density and spacing of the vibrational state cross sections.

F. HT^+

DE and DI cross sections of HT^+ in the initial state v_i are presented in Fig. 15. Results are given up to the vibrational state $v_i = 12$.

G. DT^+

Figure 16 presents the DE and DI cross sections of DT^+ in the initial state v_i. Results are given up to the vibrational state $v_i = 15$.

IV. CONCLUSION

The convergent close-coupling method has been applied to electron scattering from H_2^+ and its isotopologues within the adiabatic approximation. Vibrationally weighted proton production, deuteron production, and dissociative ionization cross sections are in excellent agreement with experimental data [3–5,7,8,14]. Dissociative excitation and dissociative ionization cross sections are also given as a function of the molecule's initial vibrational state. The results for dissociative excitation cross sections of $HD^+(1s\sigma_g,0)$ are also in excellent agreement with the measurements of Andersen *et al.* [13].

Isotopic effects on the direct electron scattering processes have been investigated for H_2^+, D_2^+, and T_2^+. Only the vibrationally weighted proton, deuteron, and triton production cross sections had a noticeable variation in the low-energy region. These isotopic effects stem from the difference in vibrational wave functions and more importantly the vibrational populations.

Both dissociative excitation and dissociative ionization cross sections were found to significantly depend on the initial vibrational state of the molecule. This dependence was seen across the entire energy range, where the major effects were at the peak of the cross section and in the intermediate-energy region.

To date, the simplest molecular system H_2^+ and its isotopologues have been scarcely studied both theoretically and experimentally. The authors would like to encourage measurements of dissociative excitation and dissociative ionization cross sections across the entire energy range for HD^+ (or one of its isotopologues) in the vibrational ground state. This would give theorists a relatively simple benchmark result to compare with.

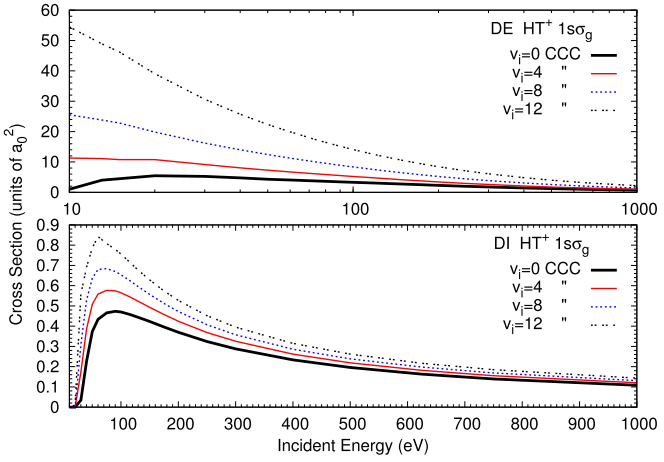

FIG. 15. (Color online) Dissociative excitation (DE) and dissociative ionisation (DI) cross sections for electron scattering from HT^+ in the electronic ground, vibrational state v_i.

ACKNOWLEDGMENTS

We would like to thank Professor L. H. Andersen and Professor L. Wolniewicz for sending us their data in electronic form. This work was supported by the Australian Research Council and Curtin University. We are grateful for access to the National Computing Infrastructure Facility and its Western Australian node iVEC. Calculations were performed on the EPIC supercomputer funded under the Pawsey Project.

[1] R. Janev, D. Reiter, and U. Samm, http://www.eirene.de/reports/report_4105.pdf.
[2] M. Fifirig and M. Stroe, J. Phys. B: At., Mol. Opt. Phys. **44**, 085202 (2011).
[3] G. H. Dunn, B. Van Zyl, and R. N. Zare, Phys. Rev. Lett. **15**, 610 (1965).
[4] G. H. Dunn and B. Van Zyl, Phys. Rev. **154**, 40 (1967).
[5] D. F. Dance, M. F. A. Harrison, R. D. Rundel, and A. C. H. Smith, Proc. Phys. Soc. **92**, 577 (1967).
[6] D. Mathur, S. U. Khan, and J. B. Hasted, J. Phys. B: At., Mol. Phys. **12**, 2043 (1979).
[7] M. O. A. El Ghazaly, J. Jureta, X. Urbain, and P. Defrance, J. Phys. B: At., Mol. Opt. Phys. **37**, 2467 (2004).
[8] B. Peart and K. T. Dolder, J. Phys. B: At. Mol. Phys. **4**, 1496 (1971).
[9] B. Peart and K. T. Dolder, J. Phys. B: At. Mol. Phys. **5**, 1554 (1972).
[10] B. Peart and K. T. Dolder, J. Phys. B: At. Mol. Phys. **5**, 860 (1972).
[11] H. Hus, F. Yousif, C. Noren, A. Sen, and J. B. A. Mitchell, Phys. Rev. Lett. **60**, 1006 (1988).
[12] F. Yousif and J. Mitchell, Z. Phys. D: At., Mol. Clusters **34**, 195 (1995).
[13] L. H. Andersen, P. J. Johnson, D. Kella, H. B. Pedersen, and L. Vejby-Christensen, Phys. Rev. A **55**, 2799 (1997).
[14] B. Peart and K. T. Dolder, J. Phys. B: At. Mol. Phys. **6**, 2409 (1973).
[15] F. von Busch and G. H. Dunn, Phys. Rev. A **5**, 1726 (1972).
[16] J. M. Peek, Phys. Rev. **140**, A11 (1965).
[17] N. van Asselt, J. Maas, and J. Los, Chem. Phys. **5**, 429 (1974).
[18] N. van Asselt, J. Maas, and J. Los, Chem. Phys. Lett. **24**, 555 (1974).
[19] J. M. Peek, Phys. Rev. **154**, 52 (1967).
[20] J. M. Peek, Phys. Rev. A **10**, 539 (1974).
[21] J. M. Peek and T. A. Green, Phys. Rev. **183**, 202 (1969).
[22] J. W. Liu, J. Phys. B: At., Mol. Opt. Phys. **22**, 2605 (1989).
[23] H. D. Hagstrum and J. T. Tate, Phys. Rev. **59**, 354 (1941).
[24] P. Baierl and W. Kiefer, J. Chem. Phys. **77**, 1693 (1982).
[25] K. Yong-Ki, K. K. Irikura, and M. A. Ali, J. Res. Natl. Inst. Stand. Technol. **105**, 285 (2000).
[26] T. Takagi, Phys. Scr. **2002**, 52 (2002).
[27] M. Stroe and M. Fifirig, J. Phys. B: At., Mol. Opt. Phys. **42**, 205203 (2009).
[28] K. Chakrabarti, D. R. Backodissa-Kiminou, N. Pop, J. Z. Mezei, O. Motapon, F. Lique, O. Dulieu, A. Wolf, and I. F. Schneider, Phys. Rev. A **87**, 022702 (2013).
[29] J. Tennyson, At. Data Nucl. Data Tables **64**, 253 (1996).
[30] J. Tennyson and C. J. Noble, J. Phys. B: At. Mol. Phys. **18**, 155 (1985).
[31] F. Robicheaux, J. Phys. B: At., Mol. Opt. Phys. **29**, 779 (1996).
[32] M. S. Pindzola, F. Robicheaux, and J. Colgan, J. Phys. B: At., Mol. Opt. Phys. **38**, L285 (2005).
[33] M. S. Pindzola, F. Robicheaux, J. A. Ludlow, J. Colgan, and D. C. Griffin, Phys. Rev. A **72**, 012716 (2005).
[34] M. C. Zammit, D. V. Fursa, and I. Bray, Phys. Rev. A **88**, 062709 (2013).
[35] I. Bray and A. T. Stelbovics, Phys. Rev. A **46**, 6995 (1992).
[36] I. Bray, Phys. Rev. A **49**, 1066 (1994).
[37] I. Bray, D. V. Fursa, A. S. Kadyrov, A. T. Stelbovics, A. S. Kheifets, and A. M. Mukhamedzhanov, Phys. Rep. **520**, 135 (2012).
[38] D. V. Fursa and I. Bray, New J. Phys. **14**, 035002 (2012).
[39] I. Bray, D. V. Fursa, A. S. Kheifets, and A. T. Stelbovics, J. Phys. B: At., Mol. Opt. Phys. **35**, R117 (2002).
[40] I. Bray and D. V. Fursa, Phys. Rev. Lett. **76**, 2674 (1996).
[41] I. Bray, Phys. Rev. Lett. **89**, 273201 (2002).
[42] D. V. Fursa and I. Bray, Phys. Rev. Lett. **100**, 113201 (2008).
[43] C. J. Bostock, J. Phys. B: At., Mol. Opt. Phys. **44**, 083001 (2011).
[44] C. J. Bostock, D. V. Fursa, and I. Bray, Phys. Rev. A **89**, 032712 (2014).
[45] I. B. Abdurakhmanov, A. S. Kadyrov, I. Bray, and A. T. Stelbovics, J. Phys. B: At., Mol. Opt. Phys. **44**, 075204 (2011).
[46] M. C. Zammit, D. V. Fursa, and I. Bray, Phys. Rev. A **87**, 020701 (2013).
[47] I. B. Abdurakhmanov, A. S. Kadyrov, D. V. Fursa, and I. Bray, Phys. Rev. Lett. **111**, 173201 (2013).
[48] I. B. Abdurakhmanov, A. S. Kadyrov, D. V. Fursa, S. K. Avazbaev, and I. Bray, Phys. Rev. A **89**, 042706 (2014).
[49] J. M. Peek, Phys. Rev. **183**, 193 (1969).
[50] J. T. Broad and W. P. Reinhardt, J. Phys. B: At., Mol. Opt. Phys. **9**, 1941 (1976).
[51] H. A. Yamani and L. Fishman, J. Math. Phys. **16**, 410 (1975).
[52] A. T. Stelbovics, Phys. Rev. A **41**, 2536 (1990).
[53] W. A. Isaacs and M. A. Morrison, Phys. Rev. A **53**, 4215 (1996).
[54] Y. Itikawa, Theor. Chem. Acc. **105**, 123 (2000).
[55] N. F. Lane, Rev. Mod. Phys. **52**, 29 (1980).
[56] D. R. Bates, K. Ledsham, and A. L. Stewart, Phil. Trans. R. Soc. Lond. A **246**, 215 (1953).
[57] D. R. Bates, J. Chem. Phys. **19**, 1122 (1951).
[58] D. M. Bishop and L. M. Cheung, J. Phys. B: At. Mol. Phys. **11**, 3133 (1978).
[59] D. R. Bates, R. T. S. Darling, S. C. Hawe, and A. L. Stewart, Proc. Phys. Soc. A **67**, 533 (1954).
[60] L. Wolniewicz and J. Poll, J. Mol. Spectrosc. **72**, 264 (1978).
[61] W. Kolos, K. Szalewicz, and H. J. Monkhorst, J. Chem. Phys. **84**, 3278 (1986).
[62] D. Wünderlich and U. Fantz, At. Data Nucl. Data Tables **97**, 152 (2011).
[63] I. Bray, I. E. McCarthy, J. Wigley, and A. T. Stelbovics, J. Phys. B: At., Mol. Opt. Phys. **26**, L831 (1993).
[64] B. Peart, D. S. Walton, and K. T. Dolder, J. Phys. B: At. Mol. Phys. **2**, 1347 (1969).
[65] F. M. Chapman, J. Chem. Phys. **63**, 2101 (1975).